Case Studies in Thermal Engineering 40 (2022) 102508

Contents lists available at ScienceDirect

Case Studies in Thermal Engineering

journal homepage: www.elsevier.com/locate/csite

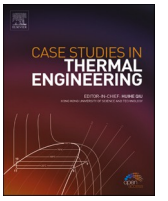

Heat transfer modelling of thermal anti-freezing method for ice hot-point drilling

Yazhou Li [a], Pavel G. Talalay [b], Xiaopeng Fan [b], Da Gong [b], Bing Li [a,*], Yuting Ye [a], Yue Wang [a], Ting Wang [b]

[a] School of Engineering and Technology, China University of Geosciences (Beijing), Beijing, 100083, China
[b] Polar Research Center, Jilin University, Changchun, Jilin, 130021, China

ARTICLE INFO

Keywords:
Hot-point drill
Thermal anti-freezing
Borehole closure
Power density
Temperature distribution

ABSTRACT

The melting water produced from ice during hot-point drilling can easily freeze and cause the hot-point drill to stick. Two different thermal anti-freezing methods exist to prevent water-filled boreholes from refreezing: the heating cable method and lateral heating method. However, the required power density and ice temperature distribution when using these two methods have not been fully discussed. In this study, heat transfer models of the two thermal anti-freezing methods were first developed based on a simplified heat conduction equation by considering the downward movement of the hot-point drill. Subsequently, case studies were conducted to determine the characteristics of the heat transfer during hot-point drilling. Finally, the variations in the power density, power consumption, borehole closure time, borehole closure length, and thermal layer thickness for both thermal anti-freezing methods were evaluated. We recommend that the heating cable method should be used to drill boreholes with shallow depths or small diameters in temperate ice, whereas the lateral heating method can be applied to a wide range of ice temperatures, borehole diameters, and borehole depths. Generally, the paper presents useful guidance for designing the heating cable and lateral heater and reducing the risk of borehole freezing.

1. Introduction

A hot-point drill (HPD), also known as a melt probe, has an electrically heated solid nose at its bottom tip to melt ice without coring. Armored power cables are typically used for HPD suspension and power delivery. Ice boreholes melted using HPDs can be used to install ablation sticks, determine ice thickness, locate englacial and subglacial streams, and measure the temperature and other internal features of glaciers [1–4]. Since its first use in 1940–1941 on the Ross Ice Shelf, Antarctica [5], more than 55 HPDs have been proposed or designed to investigate glaciers, ice caps, and ice sheets (drills were reviewed by Talalay [6]).

HPDs are used in a wide temperature range, from very cold temperatures lower than −50 °C to a temperature close to the melting point of ice [7]. In hot-point drilling, the ice beneath the HPD melts and the borehole is filled with liquid water. If the ice is temperate, the melted borehole may remain open for several days, thereby facilitating an uninterrupted drilling process. However, when drilling in cold ice, anti-freezing methods must be used to prevent the melting water from freezing. Otherwise, the borehole would become refrozen and the HPD would be stuck.

Three different methods exist to prevent ice boreholes melted using HPDs from freezing [8]. They are (1) using a hydrophilic or

* Corresponding author.
E-mail address: bing@cugb.edu.cn (B. Li).

https://doi.org/10.1016/j.csite.2022.102508
Received 15 July 2022; Received in revised form 2 October 2022; Accepted 19 October 2022
Available online 24 October 2022

hydrophobic liquid to lower the freezing point of the liquid in the borehole [9–12]; (2) removing the melting water from the borehole [13,14], and (3) using heating power to prevent meltwater from refreezing, or the thermal anti-freezing method [15–19].

As shown in Fig. 1, the thermal anti-freezing method involves two different methods. The first method involves installing a heating cable along the borehole to prevent the meltwater from refreezing. For example, a heating cable was added to a borehole drilled using an HPD on the Fox glacier, Yukon, Canada, to reduce the borehole closure rate [15]. Suto et al. recommended the use of a heating cable to allow movement of the HPD in a borehole [16]. Hereafter, the first thermal anti-freezing method is called the heating cable method (HCM). The other method allows the borehole to refreeze completely above the HPD. However, the HPD must contain a wound power cable inside, which is laid out with its descent and subsequently frozen in ice [20,21]. The instrumented HPD with a power cable is also called "freezing-in HPD." The lateral body of a freezing-in HPD typically requires electrical heating. For example, many freezing-in HPDs, such as IceMole, RECAS, and TRIPLE-IceCraft, have been instrumented with side-wall heaters [17–19]. In this paper, this method of thermal anti-freezing is called the lateral heating method (LHM). Commonly, the diameter of a freezing-in HPD changes from 6.5 to 40 cm while the length increases from 0.87 to 8 m. The penetration rate of freezing-in HPD is frequently less than 3 m/h [22]. The heating cable and lateral heater are the most important components for preventing a water-filled borehole from freezing. The key to designing a heating cable and lateral heater is determining the required power, which can be obtained by analyzing the ice temperature fields during drilling.

In the past, other borehole anti-freezing methods were used more widely compared with the thermal anti-freezing methods because of their lower power consumption. Consequently, the prevention of freezing of ice boreholes using hydrophilic or hydrophobic liquids has been well studied [23–26]. The method of removing melting water from the borehole during hot-point drilling has also been fully developed [13,14]. However, discussions on thermal anti-freezing methods for ice boreholes are scarce.

The power consumption required for the heating cable used in an exploratory ice drilling system have been estimated by neglecting its movement, which results in inaccurate results [16]. The ice temperature field during drilling and the power density distribution of the heating cable for HCM have not been discussed. Consequently, heating cables cannot be reasonably designed and used, which increases the risk of borehole closure and HPD sticking. Aamot [27] first established a model to calculate the required power density at the outer surface of a freezing-in HPD. Subsequently, this method was adopted by others [22,28]. However, this method is mathematically difficult and cannot be used to estimate ice-temperature distribution. To date, the ice temperature field around a freezing-in HPD and its borehole closure process during ice drilling have rarely been discussed, except for the brief discussion on ice-temperature distribution during thermal core drilling presented by Zagorodnov et al. [24].

In recent years, interest in exploring ice-covered aquatic environments, such as subglacial lakes in Antarctica and sub-ice oceans on extraterrestrial planets, using HPDs with thermal anti-freezing methods, has increased significantly because of their reliable drilling performance and low environmental damage [29–32]. In addition, the development of numerical techniques provides an opportunity to solve the complex mathematical problem of heat transfer [33–35]. However, as one of the keys to successfully drill to the target depth with an HPD using the thermal anti-freezing methods, related problems such as power consumption and temperature fields during ice hot-point drilling have not been fully solved.

In this paper, physical and mathematical models of the two thermal anti-freezing methods are established, which are numerically simple and can be used to precisely calculate the power consumption and temperature fields during ice hot-point drilling. Case studies are presented to illustrate the characteristics of heat transfer when using the two thermal anti-freezing methods. Finally, the changes in the different variables for HCM and LHM under different working conditions are evaluated. We believe that this paper provides practical guidelines for using thermal anti-freezing methods in ice hot-point drilling.

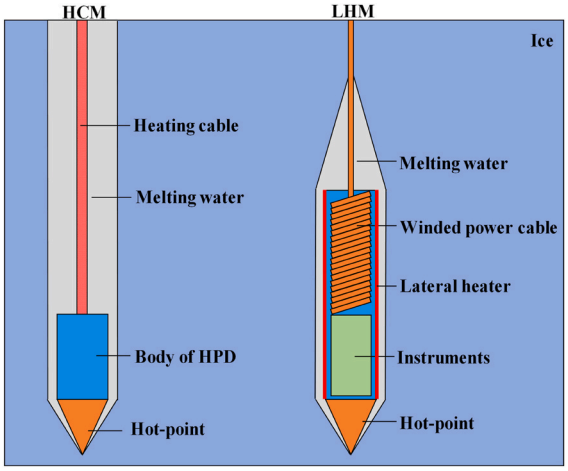

Fig. 1. Thermal anti-freezing methods for ice boreholes melted using an HPD.

2. Methodologies

2.1. Physical model

A cylindrical coordinate system (*o-rz*) is used to describe the ice hot-point drilling process. The origin of the cylindrical coordinate system is located at the bottom center of the hot point. Because of its axisymmetric geometry, only half of the HPD is studied, which simplifies the subsequent modelling process and reduces the calculation time. As shown in Fig. 2a, when the HCM is used for ice borehole anti-freeing, a heating cable with radius r_0 should always be heated at a power density of q_0 to maintain the borehole radius at R_0 during ice drilling. The heat generated by the heating cable is transferred from the melting water to the borehole wall and dissipated into the surrounding ice. As the borehole depth H increases, the increasing amount of ice around the borehole wall warms, forming a thermal ice layer. The thermal ice layer extends from the borehole wall to the ice, where the original temperature begins to increase. The thickness of the thermal ice layer δ is called the thermal layer thickness (TLT) at the drilling depth. In this paper, the ice temperature at the furthest boundary of the thermal ice layer ($r = R_0 + \delta$) is quantified to be 0.01 °C higher than the original ice temperature.

When the LHM is used, the ice around the borehole can be divided into three sections along the axial direction: anti-freezing, refreezing, and cool-down sections (Fig. 2b). The anti-freezing section has a gap between the lateral heater and borehole wall, which is expected to be very thin and can be neglected in our model. The melting water generated from the bottom of the hot point flows upward in the thin gap and forms a water cavity above the HPD. In the anti-freezing section, a lateral heater with a power density of q along its length L is used to maintain the radius of the ice borehole at the same radius of R_0 as the HPD. The heat from the lateral heater is applied to the surrounding ice during ice drilling. In the refreezing section, the melting water in the water cavity gradually refreezes until the borehole radius decreases from R_0 to 0. The length of the refreezing section is called the borehole closure length (BCL) and the time spent for melting water refreezing is called the borehole closure time (BCT). The BCL and BCT are represented by h and t_c, respectively. The TLT in the LHM represents the maximum range of the thermal ice layer when the borehole refreezes completely. In the cool-down section, the borehole is closed, and the ice temperature gradually decreases to the original temperature T_{ice}.

In both thermal anti-freezing methods, the temperature at the ice borehole wall remains at the melting point of ice T_m, whereas the ice temperature at infinity remains at its initial temperature T_{ice}. To obtain the minimum power density required by the heating cable or lateral heater, the following assumptions are made:

(1) During ice hot-point drilling, the HPD operates stably, and tilting of the HPD does not occur.
(2) The heat generated by the hot point is used for downward drilling, and the borehole is not enlarged by the power lost from the hot point.
(3) When the LHM is used, the temperature in the water cavity is uniform and remains at 0 °C.
(4) The convection of melting water can be neglected and heat transfer in the melting water is dominated by conduction when $H \gg R_0$ or $L + h \gg R_0$.

2.2. Mathematical model

In both thermal anti-freezing methods, the water and ice temperatures are governed by the following two-dimensional equations [26]:

$$\frac{\partial^2 T_w}{\partial r^2} + \frac{1}{r}\frac{\partial T_w}{\partial r} + \frac{\partial^2 T_w}{\partial z^2} = \frac{1}{\alpha_w}\frac{\partial T_w}{\partial t} \tag{1}$$

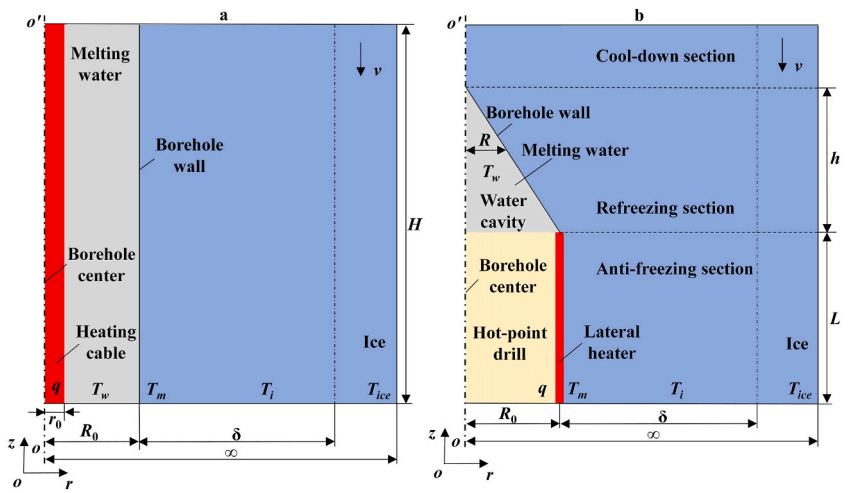

Fig. 2. Physical models of thermal anti-freezing methods: (a) HCM; (b) LHM.

$$\frac{\partial^2 T_i}{\partial r^2}+\frac{1}{r}\frac{\partial T_i}{\partial r}+\frac{\partial^2 T_i}{\partial z^2}-\frac{v}{\alpha_i}\frac{\partial T_i}{\partial z}=\frac{1}{\alpha_i}\frac{\partial T_i}{\partial t} \tag{2}$$

When $H \gg R_0$ or $L+h \gg R_0$, $\frac{\partial^2}{\partial r^2} \gg \frac{\partial^2}{\partial z^2}$ and the two equations above can be reduced to

$$\frac{\partial^2 T_w}{\partial r^2}+\frac{1}{r}\frac{\partial T_w}{\partial r}=\frac{1}{\alpha_w}\frac{\partial T_w}{\partial t} \tag{3}$$

$$\frac{\partial^2 T_i}{\partial r^2}+\frac{1}{r}\frac{\partial T_i}{\partial r}-\frac{v}{\alpha_i}\frac{\partial T_i}{\partial z}=\frac{1}{\alpha_i}\frac{\partial T_i}{\partial t} \tag{4}$$

To solve Eq. (4), the vertical downward movement of the HPD is first neglected, and its effect on the spatial distribution of the ice temperature is considered later (Eq. (9)). Here, Eq. (4) is simplified to be one-dimensional and can be described as [10,36].

$$\frac{\partial^2 T_i}{\partial r^2}+\frac{1}{r}\frac{\partial T_i}{\partial r}=\frac{1}{\alpha_i}\frac{\partial T_i}{\partial t} \tag{5}$$

The boundary condition of Eq. (5) is

$$T_i(r=R,t)=T_m \tag{6}$$

$$T_i(r=\infty,t)=T_{ice} \tag{7}$$

Additionally, its initial condition is

$$T_i(r,0)=T_{ice} \tag{8}$$

The ice temperature in the *r*-direction can be independently solved using Eqs. (5)–(8). The spatial distribution of ice temperature can then be obtained using the following equation:

$$T_{i_2D}(r,z)=T_{i_1D}\left(r,\frac{z}{v}\right) \tag{9}$$

We observe from Eq. (9) that the one-dimensional ice temperature can be transformed into a two-dimensional ice temperature by considering the movement of the HPD. In the following section, only Eq. (5) is used as the base to calculate the spatial distribution of the ice temperature.

To prevent the borehole diameter from decreasing, the heat lost to the surrounding ice during drilling is compensated using the power from the heating cable or lateral heater, and the heat flux at the water–ice interface should be

$$q(z)=-k_i\frac{\partial T_i}{\partial r}\bigg|_{r=R,t=\frac{z}{v}} \tag{10}$$

When the HCM is used, the heat flux at the water–ice interface is maintained as $q(z)(0 \le z \le H)$ to maintain the borehole diameter. Energy is conserved during heat transfer in the melting water; therefore,

$$2\pi r_0 q_0(z)=2\pi R_0 q(z) \tag{11}$$

Subsequently, the power density of the heating cable can be obtained using

$$q_0(z)=\frac{R_0 q(z)}{r_0}=-k_i\frac{R_0}{r_0}\frac{\partial T_i}{\partial r}\bigg|_{r=R_0,t=\frac{z}{v}} \tag{12}$$

The total power consumed by the heating cable can be estimated as

$$Q=2\pi r_0\int_0^H q_0(z)dz \tag{13}$$

Considering the ice temperature at time *t* as a reference time framework, the water temperature at *t* is in a steady state, and Eq. (3) can be reduced to

$$\frac{d^2 T_w}{dr^2}+\frac{1}{r}\frac{dT_w}{dr}=0(r_0 \le r \le R_0) \tag{14}$$

After integration, Eq. (14) becomes

$$T_w=a\ln r+b \tag{15}$$

The temperature of water and ice at the borehole wall is consistent; thus,

$$T_w(r=R_0)=T_m \tag{16}$$

At the outer surface of the heating cable, the power density can be expressed as

$$q_0(z) = k_w \left.\frac{dT_w}{dr}\right|_{r=r_0} \tag{17}$$

Substituting Eqs. (16) and (17) into Eq. (15), we obtain $a = \frac{-R_0 q(z)}{k_w}$, $b = \frac{R_0 q(z)}{k_w} ln\, R_0 + T_m$. The water temperature in the borehole can then be calculated as

$$T_w = \frac{R_0 q(z)}{k_w} ln \frac{R_0}{r} + T_m \tag{18}$$

When the LHM is used, the power density along the freezing-in HPD is

$$q_0(z) = q(z) (0 \le z \le L) \tag{19}$$

The total power consumed by the "freezing-in HPD" is calculated using the following equation:

$$Q = 2\pi R_0 \int_0^L q_0(z) dz \tag{20}$$

In the refreezing section, the melting water in the borehole is gradually refrozen, which means that the refreezing rate of the borehole wall $\frac{dR}{dt}$ can be estimated using

$$k_i \left.\frac{\partial T_i}{\partial r}\right|_{t=\frac{z}{v}} = \rho_i L_m \frac{dR}{dt} \ (L \le z \le L + h) \tag{21}$$

Subsequently, the borehole above the freezing-in HPD at position z can be described as

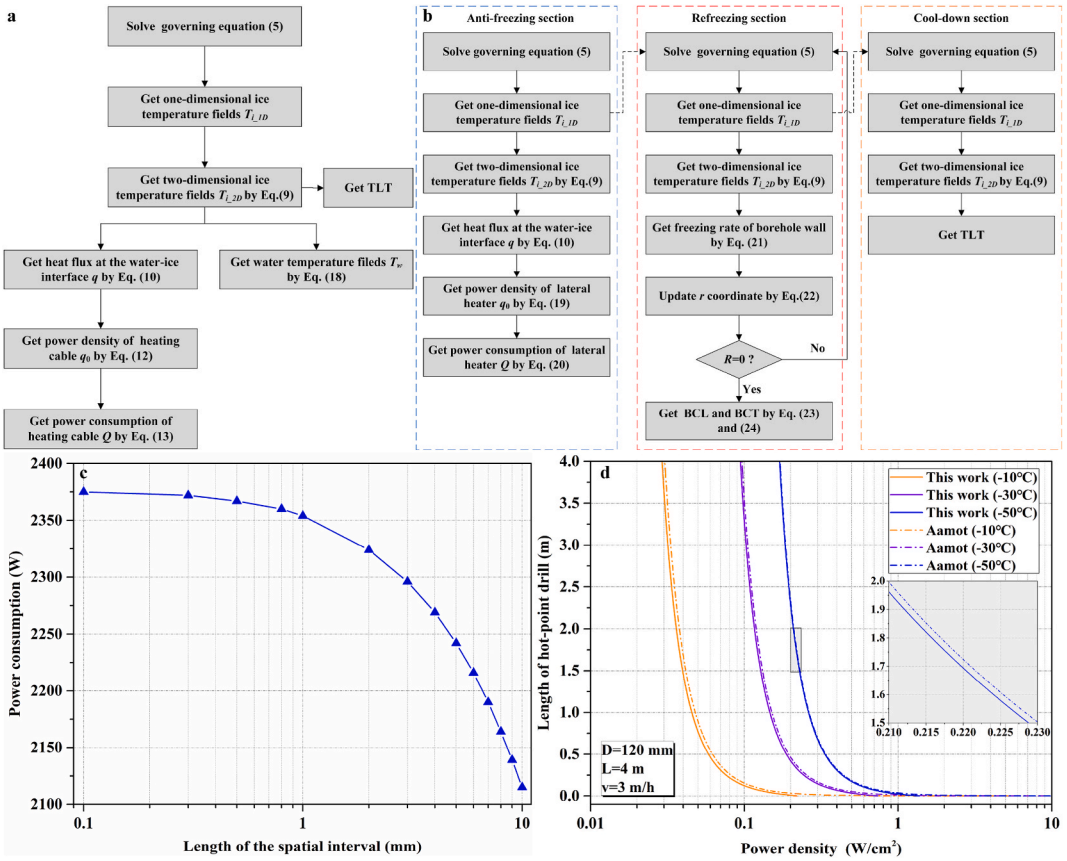

Fig. 3. (a) Flow diagram for calculating the HCM model; (b) flow diagram for calculating the LHM model; (c) independence verification of the length of the intervals; (d) comparison of our model with Aamot's method.

$$R(z) = R_0 + \int_0^{\frac{z-L}{v}} \left(\frac{dR}{dt}\right) dt \ (L \le z \le L+h) \tag{22}$$

The BCT and BCL can be calculated using the following expressions

$$R_0 = -\int_0^{t_c} \left(\frac{dR}{dt}\right) dt \tag{23}$$

$$h = t_c v \tag{24}$$

In the cool-down section, the ice temperature is still governed by Eq. (5), and the borehole diameter becomes zero.

2.3. Model solving and validation

As shown in Fig. 3a, for the HCM, the one-dimensional ice temperature is first calculated using the governing equation (5). Subsequently, two-dimensional ice temperature fields are obtained by considering the downward movement of the HPD. Consequently, the TLT and temperature of the melting water in the borehole could be easily obtained. The heat flux at the borehole wall is estimated based on the ice temperature distribution. Finally, the required power density of the heating cable and its total power consumption are calculated.

For the LHM, three steps are required to calculate the proposed model (Fig. 3b). First, the ice temperature in the anti-freezing section is calculated to evaluate the power density of the lateral heater. In this step, the calculation order is almost the same as that for the LHM. Subsequently, the ice temperature at the end of the anti-freezing section is set as the initial condition to solve the ice temperature in the refreezing section. In the second step, the refreezing rate of the borehole wall is calculated according to the ice temperature gradient at the borehole wall. The borehole diameter is then updated in each calculation step until the borehole completely refreezes. Finally, the BCL and BCT are obtained according to the time spent for borehole refreezing. In the final step, the ice temperature in the cool-down section is obtained using the ice temperature at the end of the refreezing section as the initial condition. As a result, the TLT for the LHM can be easily obtained.

All the equations above were calculated using MATLAB R2014b, which is widely used to solve mathematical problems of heat transfer [37–39]. In the calculations, the distance from the borehole wall to the point where the ice temperature was always maintained as T_{ice} was set to 100 times the borehole diameter, which was confirmed to be sufficiently long using later calculations. The differential Eq. (5) was numerically calculated using the common central difference method. In the calculations of Eq. (5), the spatial r coordinate was discretized into small intervals, whereas the time was discretized into very short steps. In our model, the spatial distance was discretized into small intervals with a length of 1 mm and the time step was set to 1 s.

The independence of the spatial interval length was verified to evaluate its effect on the calculation results. In the independence verification, a freezing-in HPD with a diameter of 120 mm and a length of 4 m was used to drill −30 °C ice at a penetration rate of 3 m/h. The length of the spatial intervals was assumed to change from 0.1 to 10 mm. As shown in Fig. 3c, the calculated power consumption of the freezing-in HPD gradually increased from 2115 to 2353 W when the length of the spatial intervals decreased from 10 to 1 mm. However, when the length of the spatial intervals continued decreasing to 0.1 mm, the power consumption increased by only 17 W, which was less than 1% of the total power consumption. In our model, spatial intervals with lengths shorter than 1 mm significantly increase the calculation time; thus, 1 mm is the recommended reasonable length of the spatial intervals.

As shown in Fig. 3d, the power density of the freezing-in HPD at different ice temperatures was calculated and compared with the results of Aamot's method to validate our model [27]. The freezing-in HPD had a diameter of 120 mm and length of 4 m, while the rate of penetration (ROP) was assumed to be 3 m/h. The power density calculated using Aamot's method was slightly higher than that of our model. When the ice temperature decreased, the discrepancy between our model and Aamot's method decreased. For example, the maximum difference between our model and Aamot's method was 3.8% at an ice temperature of −10 °C, whereas the maximum difference decreased to 0.4% at an ice temperature of −50 °C.

For our calculations, the thermophysical parameters of ice and water are listed in Table 1 [40].

Table 1
Thermophysical parameters of the ice and water.

Parameters	Value	Unit
ρ_i	917	kg/m^3
ρ_w	1000	kg/m^3
C_i	152.5 + 7.122(T_i+273.15)	kJ/(kg·K)
C_w	4.218	kJ/(kg·K)
k_i	9.828exp(-0.0057(T_i+273.15))	W/(m·K)
k_w	0.6	W/(m·K)
L_m	333.5	kJ/kg
T_m	173.15	K

2.4. Case study

2.4.1. Case study of the HCM

To study the distribution characteristics of power density and the temperature of water and ice for the HCM, an HPD with a diameter of 50 mm and ROP of 3 m/h was used to drill ice at a temperature of −10 °C. The borehole depth was assumed to be 100 m and the diameter of the heating cable was set to 10 mm.

2.4.2. Distribution of the power density

Fig. 4a shows the variation in the power density at the borehole wall and heating cable for the HCM. The minimum power density required by the heating cable to prevent the borehole wall from refreezing first increased gradually with increasing borehole depth and then increased rapidly near the bottom of the borehole. This was because the ice near the bottom of the borehole was not sufficiently warmed by the heating cable, which were proven by the ice temperature fields. The heat flux at the borehole wall exhibited the same trend as the power density required by the heating cable. However, the heat flux at the borehole wall was five times lower than the power density of the heating cable because the borehole diameter was five times larger than the diameter of the heating cable. In this case, the total power consumed by the heating cable to prevent the 100 m borehole from freezing was approximately 4259 W.

2.4.3. Distribution of the ice and water temperature

The temperature variations of water and ice with time at different radial distances from the borehole center are shown in Fig. 4b. The water temperature continued to decrease with time, while the ice temperature continued to increase, which was the result of heat transfer from water to ice. Initially, both water and ice temperatures varied significantly. Subsequently, the rate of variation decreased. For example, the water temperature at the outer surface of the heating cable decreased by approximately 55 °C from $t = 0$ h to $t = 2$ h, whereas it decreased by only 9.4 °C from $t = 2$ h to $t = 30$ h; conversely, the temperature of the ice at a distance of 35 mm from the borehole center increased by 8.32 °C from $t = 0$ h to $t = 2$ h, whereas it increased by only 0.64 °C from $t = 2$ h to $t = 30$ h. In the initial stage, the temperature difference between the melting water and ice was considerably large; thus, the rate of heat conduction from melting water to ice was higher, and the variation in their temperature was significant. However, the temperature difference decreased after 2 h. Consequently, the variation rate of the temperature also decreased.

The ice near the borehole wall had a higher rate of temperature increase than the ice far from the borehole wall, which was caused by energy dispersion during heat transfer in the ice. For example, the ice at a distance of 35 mm from the borehole center was heated to −1.02 °C within 33.3 h, whereas the ice temperature at a distance of 305 mm from the borehole center increased to only −7.54 °C.

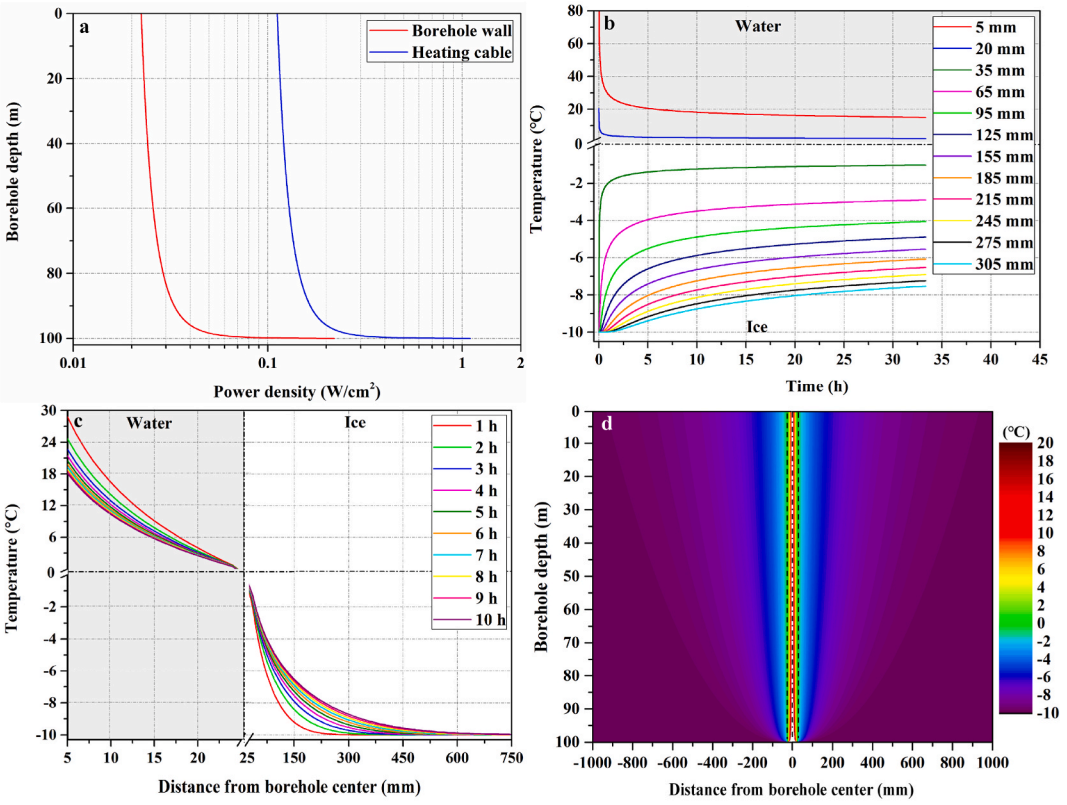

Fig. 4. (a) Power density at the borehole wall and heating cable; (b) temperature variation of water and ice with time at different distances from the borehole center; (c) temperature variation of water and ice in the radial direction at different times; (d) temperature fields for the HCM.

The heat generated by the heating cable was gradually transferred from the borehole wall to the surrounding ice. When the heat arrived at the ice, the temperature of the ice began to increase; therefore, the closer the ice is to the borehole wall, the less time it requires for the ice temperature to begin increasing. In this case, it took approximately 1.8 h for the heat generated by the heating cable to be transferred to the ice at a distance of 305 mm from the borehole center.

As shown in Fig. 4c, the water temperature gradually decreased to 0 °C from the outer surface of the heating cable to the borehole wall. The ice temperature initially decreased rapidly with an increase in the radial distance to the borehole center, and then the rate of decrease decreased. For example, at $t = 2$ h, the ice temperature decreased by 7.92 °C when its distance to the borehole center increased from 25 to 150 mm, whereas it decreased by only 1.75 °C when the distance to the borehole center increased from 150 to 300 mm. The reason for the larger decrease in the ice temperature near the borehole wall was the larger initial temperature difference, which resulted in a higher rate of heat transfer. In this case, the TLT was approximately 1466 mm, which was approximately 30 times the borehole radius.

The temperature fields of water and ice when the borehole depth reached 100 m for the HCM are shown in Fig. 4d, where the borehole wall is represented by dashed lines. The temperature gradient of ice near the borehole wall was much higher than that far

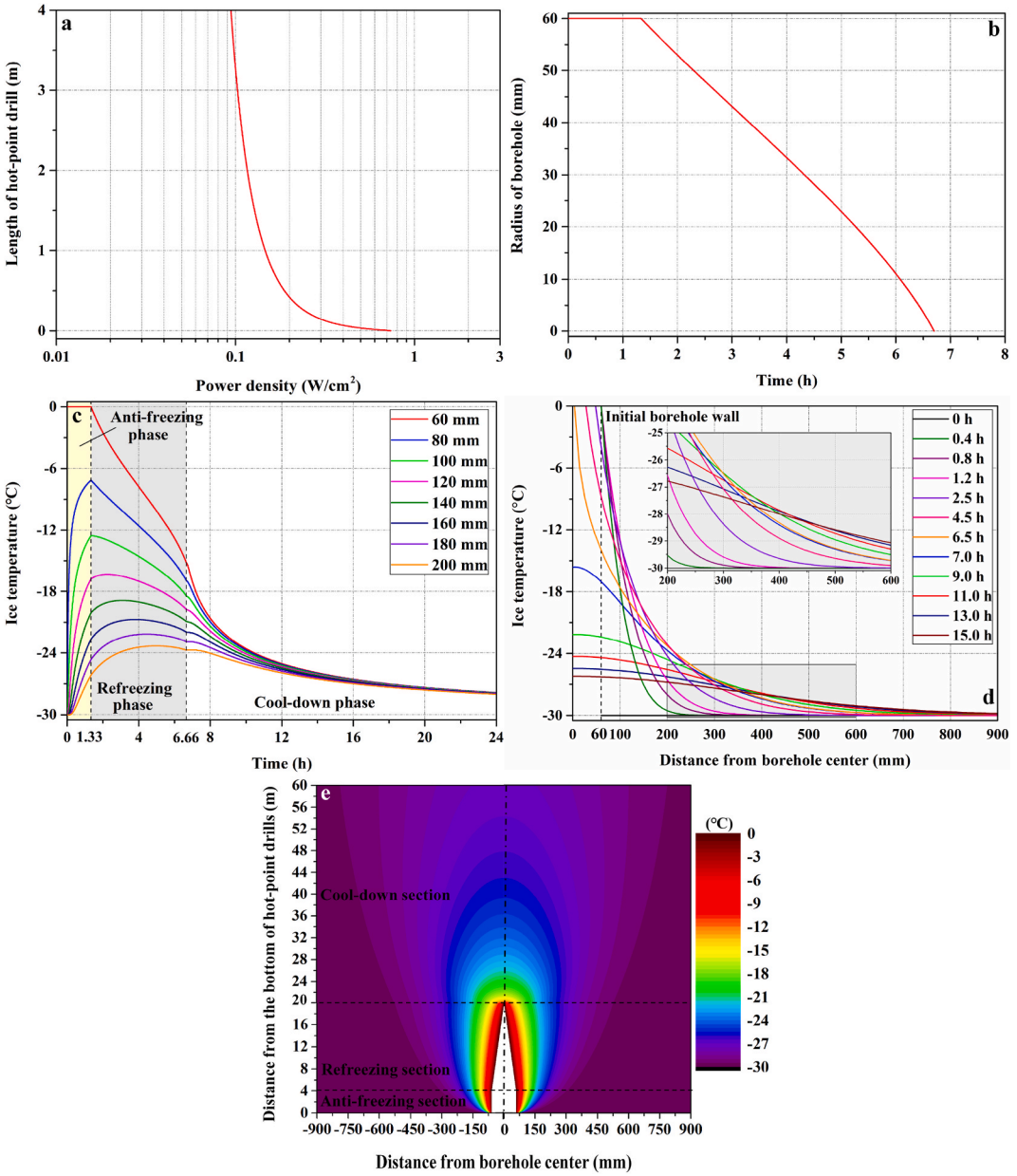

Fig. 5. (a) Power density of the lateral heater; (b) variation in the borehole radius with time; (c) variation in ice temperature with time at different radial distances from the borehole center; (d) variation in the ice temperature in the radial direction at different times; (e) ice temperature fields for the LHM.

from the borehole wall. The ice near the top of the borehole is always heated by a heating cable after drilling begins, whereas the ice near the bottom of the borehole is only heated when the HPD drills are at its position. Consequently, ice at a greater borehole depth has a lower temperature at the same radial distance. In our case, the isotherm of ice near the borehole wall was almost vertical when the borehole depth was less than 90 m. With increasing radial distance, the isotherm of ice gradually became parabolic.

2.5. Case study of the LHM

As a case study of the LHM, a freezing-in HPD with a diameter of 120 mm and length of 4 m was assumed to drill ice at −30 °C. The HPD was assumed to have an ROP of 3 m/h.

2.5.1. Distribution of power density

As shown in Fig. 5a, the power density required by the lateral heater for the LHM exhibited trends similar to those of the heating cable in the HCM case. The minimum power density required at the bottom of the lateral heater was approximately 0.737 W/cm^2. When the distance to the bottom of the borehole increased to 0.42 m, the power density rapidly decreased to 0.2 W/cm^2. As the distance to the bottom of the borehole increased, the power density decreased to 0.094 W/cm^2 at the top of the lateral heater. For the LHM, the ice near the bottom of the borehole was not sufficiently warmed; thus, it was much colder than the ice at the top of the borehole. Consequently, a much larger power density was required to prevent the borehole wall from freezing. In this case, the total power consumed by the lateral heater was 2115 W.

2.5.2. Variation in borehole radius

As shown in Fig. 5b, the radius of the drilled borehole remained at 60 mm for 1.33 h when a lateral heater was used to prevent the borehole from closing. Subsequently, the borehole radius decreased. Initially, the rate of decrease in the borehole radius was relatively low. Subsequently, the rate of decrease increased. The discussion above implies that the water-filled ice borehole with smaller diameter has a higher freezing rate at the same ice temperature. In this case, it took approximately 5.37 h for the borehole to completely refreeze, which resulted in a BCL of 16.11 m.

2.5.3. Distribution of ice temperature

As shown in Fig. 5c, the ice temperature variation can be divided into three stages: anti-freezing, refreezing, and cool-down phases. In the anti-freezing phase, the borehole wall was heated using a lateral heater, and the borehole diameter was maintained at 120 mm. The anti-freezing phase started at the beginning of ice drilling until the borehole depth reached the length of the HPD. In this case, the anti-freezing phase lasted from $t = 0$ h to $t = 1.33$ h. In the refreezing phase, the borehole wall was heated by a lateral heater and the borehole diameter began to decrease until the melted water in the borehole completely refroze. In this case, the refreezing phase began at $t = 1.33$ h and ended at $t = 6.66$ h. In the cool-down phase, the heat from the melting water completely disperses into the surrounding ice, and then the heat from the cold ice at infinity begins to transfer inward to cool the relatively warm ice near the original borehole center. The cool-down phase lasts for a long period until the ice in the borehole center returns to its initial temperature before drilling. In this case, the cool-down phase did not end even at $t = 24$ h.

In the anti-freezing phase, the ice temperature initially increases rapidly, and then the increase rate decreases, which is a consequence of the decreased temperature gradient with time. Similar to the HCM case, the further the ice was from the borehole wall, the more time was required for the heat to be transferred to its position. During heat transfer from the borehole wall to further ice, some heat was dispersed. As a result, the ice close to the borehole walls had a higher temperature than that far from the borehole walls. The ice temperature at a distance of less than 120 mm from the borehole center stopped increasing when the anti-freezing phase ended. However, the temperature of farther ice continued to increase in the refreezing phase and even in the cool-down phase. The temperature variation of ice far from the borehole center lagged behind that of ice closer to the borehole center. This was because the heat from the lateral heater required more time to be transferred to the farther ice. Note that the ice temperature at the borehole wall would always remain at the melting point in the anti-freezing phase.

In the refreezing phase, the temperature of the ice close to the borehole wall decreases rapidly, whereas the temperature of the ice farther away first increases to a maximum and then begins to decrease. Ice closer to the borehole wall has a higher rate of temperature decrease than ice farther from the borehole wall. In our case, the boundary between the close ice and far ice was at $r = 120$ mm.

In the cool-down phase, the ice temperature continues to decrease and the rate of decrease is lower than that in the refreezing phase. In this case, the temperature of the ice at different positions became nearly the same after drilling started for 16 h, and then the ice temperature began to decrease at the same rate.

The variation in ice temperature in the radial direction at different times for the LHM is shown in Fig. 5d. In the anti-freezing phase, an increasing amount of ice around the borehole wall was warmed and the ice temperature continued to increase over time. At the end of the anti-freezing phase, the frontier of the thermally disturbed ice advanced to approximately 350 mm from the borehole center.

As mentioned earlier, in the refreezing phase, the melting water in the borehole gradually freezes into ice from the borehole wall to the borehole center, and the borehole becomes increasingly smaller. Additionally, the temperature of the ice near the borehole wall begins to decrease, whereas the temperature of the other ice continues to increase. At the end of the refreezing phase, the ice within 650 mm of the borehole center is thermally disturbed.

In the cool-down phase, the heat from the warm ice continues to be transferred far away and the ice temperature continues to decrease. Later, most of the heat is dissipated in the ice, and the temperature variation of the ice far from the borehole center becomes considerably small. For example, the temperature of ice at $r = 600$ mm decreased from 29.75 to 29.00 °C in the cool-down phase. For the LHM, the TLT was 869 mm, which was approximately 7.2 times the borehole diameter.

As shown in Fig. 5e, the ice temperature fields for the LHM contained anti-freezing, refreezing, and cool-down sections. Generally,

the farther the borehole wall, the lower the ice temperature. As the distance to the borehole wall increased, the gradient of ice temperature also decreased. In the anti-freezing section, the ice close to the bottom of the borehole had a lower temperature than that in the upper part at the same radial distance, which was the result of the shorter heating time of the lateral heater. The refreezing section had a length of 16.11 m and the water cavity above the HPD had a conical shape. In the refreezing section, the isotherm of ice near the water cavity was almost parallel to the borehole wall. Compared with the ice temperatures in the other two sections, the ice temperature, as well as the gradient of ice temperature in the cool-down section, was lower. Generally, the isotherms of ice resembled spindles of different lengths that stood vertically at the bottom of the borehole.

3. Results and discussion

To investigate the variations in power density, power consumption, BCT, BCL, and TLT, a series of calculations was performed with different HPD diameters, borehole depths, or lengths of HPD, ROPs, and ice temperatures. When the HCM was used, the diameter of the heating cable was assumed to be 10 mm, and the other parameters used in the calculations are shown in the following figures.

3.1. Variation in the power density

As shown in Fig. 6a, the power density required for the heating cable increased when the diameter of the HPD increased from 30 to 70 mm. The rate of increase decreased with an increase in the HPD diameter. In practice, when the HCM is used, the temperature gradient at the water–ice interface of a smaller borehole is larger than that of a larger borehole because the borehole wall with a smaller diameter is much closer to the heating cable. Consequently, the heat flux at the borehole wall always decreases with increasing borehole diameter; however, the diameter of the heating cable remains the same. Consequently, the ratio between the power density at the heating cable and the heat flux at the borehole wall increases, which increases the power density of the heating cable with increasing diameter of the HPD.

As the borehole depth increased, the required power density of the heating cable on ice with the same depth decreased because the surrounding ice was warmed (Fig. 6b). In drilling engineering, the heating cable is always injected into the hole following the descent of the HPD; therefore, the newly injected heating cable is permitted to have a lower power density, while the pre-injected heating cable can maintain its power density and be lowered.

An increase in the ROP can result in an increase in the required power density of the heating cable (Fig. 6c). This is because a higher penetration rate implies a shorter heating time of ice during drilling; thus, the ice around the borehole wall has a colder temperature and requires a higher power density to be warmed. The rate of increase in power density gradually decreases with increasing ROP.

As shown in Fig. 6d, the power density at the heating cable decreased almost linearly with an increase in ice temperature. For example, the required power density of the heating cable at the ice surface decreased from 0.172 W/cm^2 at −15 °C to 0.055 W/cm^2 at −5 °C.

For the LHM, the required power density of the lateral heater decreased with an increase in the diameter of the HPD, and the rate of decrease gradually decreased (Fig. 7a). As shown in Fig. 7b, when the HPD length increased, the newly added lateral heater located at the upper part of the HPD had a lower power density, whereas the required power density at the lower part remained the same.

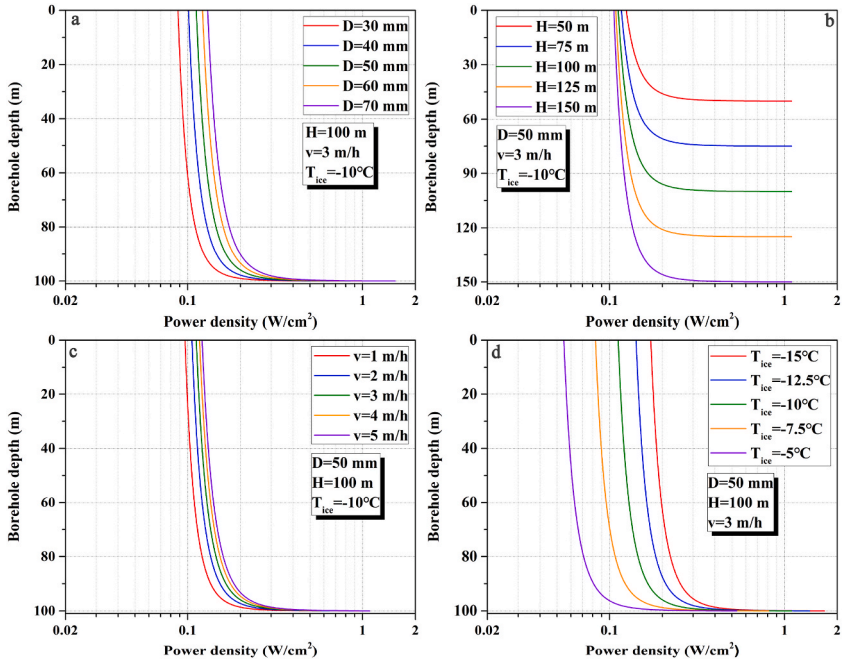

Fig. 6. Variation in the power density at the heating cable with: (a) diameter of the HPD; (b) borehole depth; (c) ROP; (d) ice temperature for the HCM.

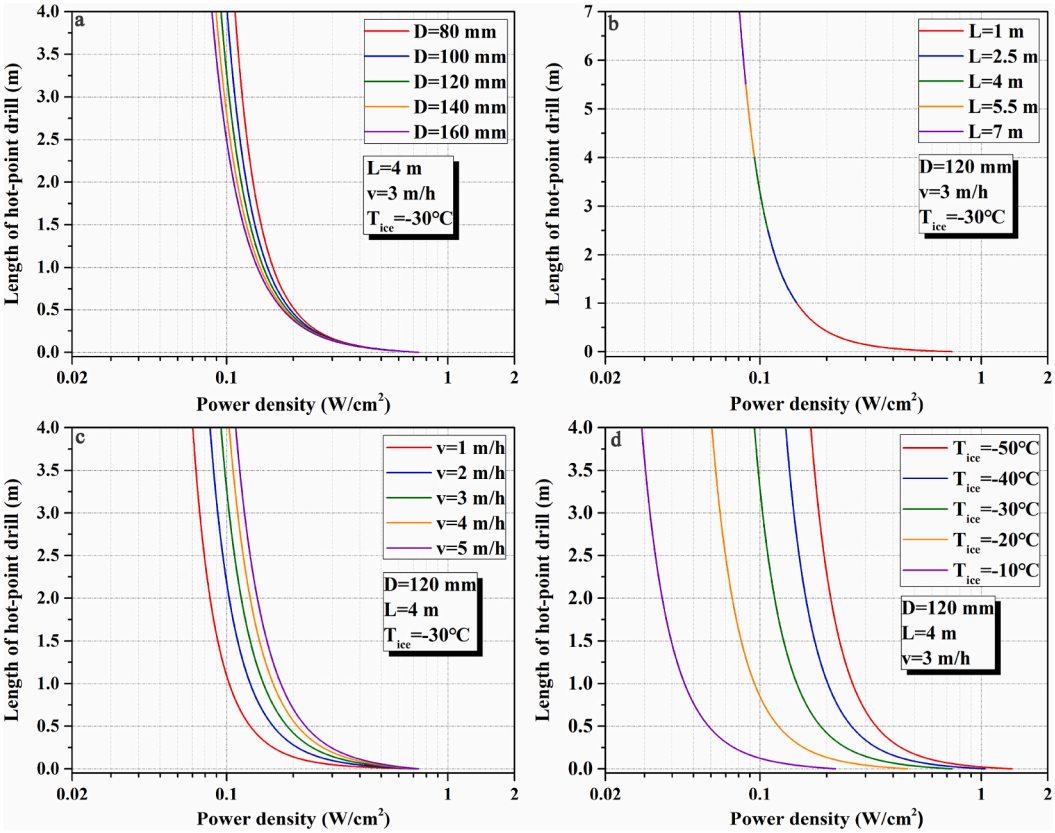

Fig. 7. Variation in the power density at the lateral heater with: (a) diameter of the HPD; (b) length of the HPD; (c) ROP; (d) ice temperature for the LHM.

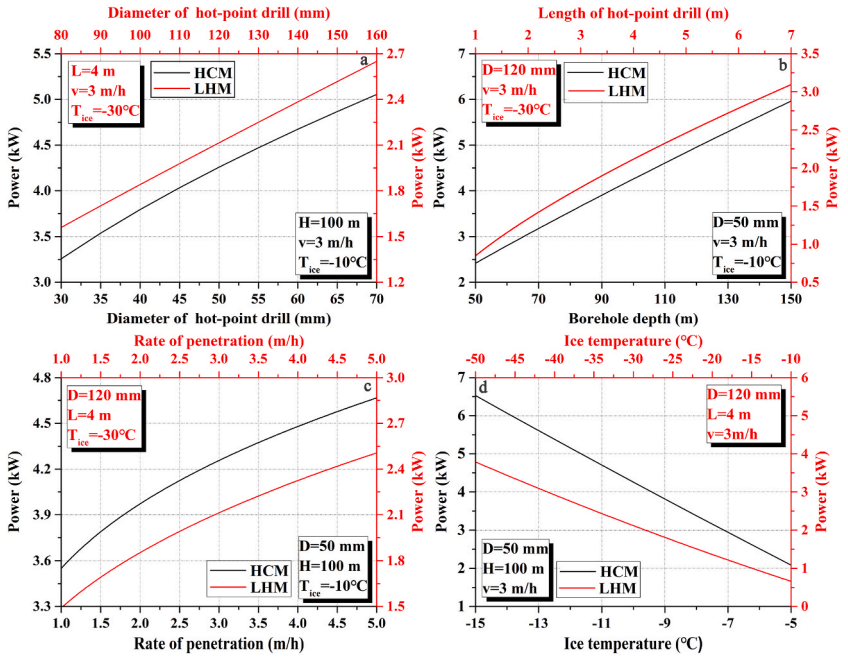

Fig. 8. Variation in the power consumption with: (a) diameter of the HPD; (b) borehole depth or length of the HPD; (c) ROP; (d) ice temperature.

Compared with the power density at the heating cable for the HCM, the power density at the lateral heater for the LHM exhibited similar variation trends with the ROP and ice temperature (Fig. 7c and d).

3.2. Variation in the power consumption

As shown in Fig. 8, the power consumption of the lateral heater for the HCM and the power consumption of the heating cable for the LHM exhibited similar variation trends. As the diameter of the HPD increased, the power consumption for both the thermal anti-freezing methods increased almost linearly (Fig. 8a). Although a larger HPD diameter resulted in a lower power density at the borehole wall, the area of the heating surface increased with an increase in the diameter of the HPD. Consequently, the total power consumption increased with the diameter of the HPD.

For the HCM, the power consumption increased almost linearly with borehole depth (Fig. 8b). However, for the LHM, the power consumption first increased rapidly with the length of the HPD, and then the rate of increase decreased. This was because the power density at the lower portion of the lateral heater was much higher than that at the higher portion.

As shown in Fig. 8c, the power consumed by the lateral heater or heating cable continued to increase with the ROP in both thermal anti-freezing methods because of their increased power density. A smaller ROP corresponds to a higher rate of increase in power consumption. Consistent with common sense, the power consumption decreased linearly with an increase in ice temperature (Fig. 8d). For example, for HCM, the power consumption of heating cable decreased from 6.5 to 2.1 kW when the ice temperature increased from −15 to −5 °C. Similarly, for the LHM, the power consumption of lateral heater decreased from 4.7 to 0.6 kW when the ice temperature increased from −50 to −10 °C.

In remote polar regions, the power sources are limited. Within a reasonable power input, the HCM can be used only to drill boreholes with shallow depths or small diameters in temperate ice. The diameter of the HPD using the HCM is recommended to be less than 70 mm, while the borehole depth should be less than 150 m. In addition, when the HCM is used, the ice temperature is recommended to be higher than −15 °C. However, the LHM can be applied to a wide range of ice temperatures, borehole diameters, borehole depths, and ROP.

3.3. Variation in the BCT and BCL

The BCT and BCL increased almost linearly with the diameter of the HPD, which was consistent with the common sense that larger boreholes require more time to be frozen (Fig. 9a). For example, when the diameter of the HPD increased from 80 to 160 mm, the BCT increased from 2.9 to 8.5 h whereas the BCL increased from 8.7 to 25.5 m.

When the length of the HPD increased, both BCT and BCL increased because a longer HPD had more time to warm the surrounding ice at the same ROP, and the melting water surrounded by the warmer ice required more time to refreeze (Fig. 9b). The increasing rates of the BCT and BCL with HPD length were relatively high when the length of the HPD was small. The rates of increase in the BCT and BCL decreased with increasing HPD length.

As shown in Fig. 9c, when ROP increased, the BCT continued to decrease, and the rate of decrease gradually decreased. Compared with an HPD with a low ROP, an HPD with a high ROP has a shorter time to heat the surrounding ice; therefore, relatively colder ice

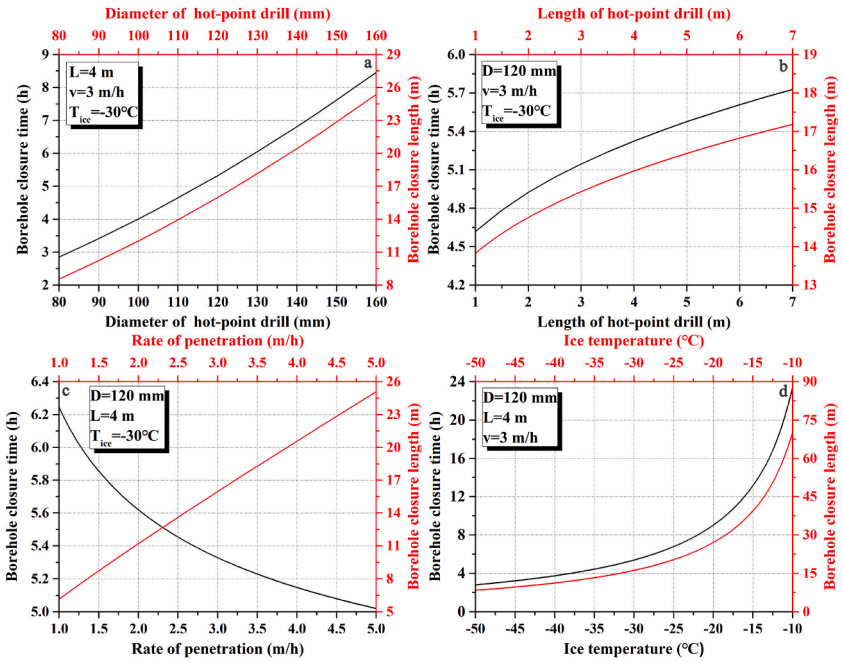

Fig. 9. Variation in the BCT and BCL with: (a) diameter of the HPD; (b) length of the HPD; (c) ROP; (d) ice temperature for the LHM.

exists near the borehole wall. Consequently, the melted water in the water cavity has a higher refreezing rate, and a shorter BCT can be obtained. The BCL is a product of the BCT and ROP. Although the BCL decreases with increasing ROP, BCL continues to increase with an increase in the ROP, which is the combined result of decreased BCT and increased ROP.

When the ice temperature was lower than −20 °C, the BCT and BCL increased gradually as the ice temperature increased (Fig. 9d). However, when the ice temperature was higher than −20 °C, the rate of increase of the BCT and BCL became significantly large. We assumed that the melted borehole may require a long time to be completely refrozen when the HPD is used in temperate glaciers or the lower portion of polar ice sheets.

3.4. Variation in the TLT

In both thermal anti-freezing methods, the TLT increased linearly with the diameter of the HPD (Fig. 10a). For the HCM, the TLT increased by only 45 mm when the diameter of the HPD increased from 30 to 70 mm. For the LHM, the TLT increased by 330 mm when the diameter of the HPD increased from 80 to 160 mm. When the HCM was used, the time spent for heat transfer in ice was the drilling time, which was the same for different HPD diameters. Therefore, we assumed that the increase in TLT with the HPD diameter for the HCM was caused by the lower heat flux of the borehole wall at larger HPD diameters. For the LHM, a larger borehole diameter requires more time to refreeze. Correspondingly, the time required for heat transfer in ice increases and heat can be further transferred.

In both thermal anti-freezing methods, the TLT increased with an increase in the HPD length or borehole depth, which was caused by the time increase in the heat transfer in ice (Fig. 10b). Initially, the increasing rate of the TLT was higher but later became slower. For the HCM, the increase in time for heat transfer in ice is due to the increased drilling time. For the LHM, both the time spent in the anti-freezing and refreezing phases increased with increasing HPD length, which subsequently resulted in a longer heating time for the surrounding ice.

As shown in Fig. 10c, the TLT decreased rapidly at a small ROP and decreased gradually at a large ROP. This phenomenon can be explained by the decreased heating time of surrounding ice at high penetration rates.

The ice temperature had opposite effects on the TLT for the HCM and LHM (Fig. 10d). When the ice temperature increased, the thermal conductivity of ice decreased, and thus, the TLT decreased for the HCM. For the LHM, the decrease in the ice thermal conductivity can also result in a decrease in the TLT. However, when the LHM is used, the increased ice temperature increases the time for borehole refreezing to increase simultaneously, which can significantly increase the time for heat transfer to the farther ice. For both the thermal anti-freezing methods, the variation rate of the TLT on cold ice is lower than that on warm ice.

Generally, the TLT is highly dependent on the time required for ice heating. If there is a sufficient heating time, the TLT can be very large. To study the required power density and temperature distribution in hot-point drilling theoretically or experimentally, the boundary condition of the ice temperature should be sufficiently large to avoid confusion caused by incorrect results.

3.5. Sensitivity analysis

As listed in Table 2, an orthogonal analysis was designed to evaluate the influence of variables such as the diameter of the HPD, borehole depth, ROP, and ice temperature on the power density, power consumption, and TLT for the HCM. In the orthogonal analysis, each of the four variables had three levels; therefore, a standard orthogonal table in the form of $L_9(3^4)$ was used, and nine calculations

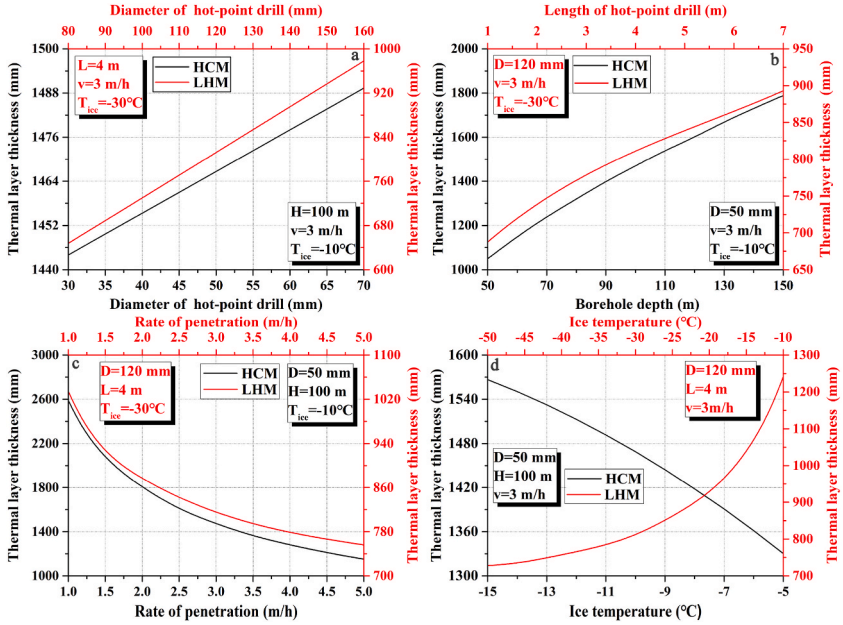

Fig. 10. Variation in the TLT with: (a) diameter of HPD; (b) borehole depth or length of the HPD; (c) ROP; (d) ice temperature.

Table 2
Design and results of the orthogonal analysis for the HCM.

No.	Variables				Results		
	D (mm)	H (m)	v (m/h)	T_{ice} (°C)	q_0 (W/cm^2)	Q (kW)	δ (mm)
1	30	50	1	−15	0.128	2.354	1880
2	30	100	3	−10	0.088	3.256	1451
3	30	150	5	−5	0.044	2.426	1240
4	50	50	3	−5	0.061	1.182	950
5	50	100	5	−15	0.186	7.156	1230
6	50	150	1	−10	0.092	5.043	3041
7	70	50	5	−10	0.160	3.248	840
8	70	100	1	−5	0.054	2.034	2282
9	70	150	3	−15	0.188	10.780	1930

were required. In the orthogonal analysis, the diameter of the HPD changed from 30 to 70 mm, whereas the borehole depth changed from 50 to 150 m. The ROP of the HPD was assumed to be in the range of 1–5 m/h and the ice temperature was assumed to increase from −15 to −5 °C. In the analysis, the power density required at the top of the heating cable, power consumption, and the TLT were calculated.

The common range analysis method was used to evaluate the effects of the four variables on the power density, power consumption, and TLT. As shown in Table 3, ice temperature had the greatest influence on the power density, whereas borehole depth had the least influence. The effects of the four variables on power consumption can be ordered as follows: ice temperature > borehole depth > HPD diameter > ROP. The ROP had a significant influence on the TLT, whereas the influences of the other variables on the TLT were smaller.

Generally, the power consumption during ice drilling with an HCM is governed by the ice temperature. For the HCM, the required power density of the heating cable is equal to the rate of heat transfer at the borehole wall, which depends on the thermal conductivity and temperature gradient. The thermal conductivity of ice is almost constant; therefore, the rate of heat transfer in ice is primarily governed by the ice temperature. The TLT is the longest distance at which heat is conducted on ice. Typically, the TLT depends on the rate of heat transfer and the time required for heat transfer. The rate of heat transfer is governed by the thermal conductivity of ice, which varies slightly with the ice temperature. For the HCM, the time used for heat transfer is equal to the drilling time, which depends on the ROP and borehole depth.

Similar to the HCM case, the same orthogonal table with the form of $L_9(3^4)$ was used to evaluate the effects of the diameter of the HPD, length of the HPD, ROP, and ice temperature on the power density at the top of the lateral heater, power consumption, TLT, BCT, and BCL for the LHM (Table 4). In the orthogonal analysis, the diameter of the HPD increased from 80 to 160 mm, whereas the length of the HPD ranged from 1 to 7 m. The ROP of the HPD was assumed to have a range of 1–5 m/h and the ice temperature changed from −50 to −10 °C.

For the LHM, the same range analysis method was used for sensitivity analysis of the four variables mentioned above. As shown in Table 5, the ice temperature had the greatest influence on all parameters of the results. The influence of the HPD length and ROP on the power density was greater than that of the HPD diameter. The influence of the four variables on the power consumption was of the same order in the cases of HCM and LHM. The ice temperature had the greatest influence on the BCT, whereas the diameter had the second greatest influence. Variations in the ROP and length of the HPD had a slight influence on the BCT. For the LHM, the contributions of the four variables to the BCL can be sorted as follows: ice temperature > ROP > HPD length > HPD diameter. In contrast to the HCM, the ice temperature and diameter of the HPD were the main variables that affected the TLT, whereas the length of the HPD and ROP had a smaller influence on the TLT.

4. Conclusions

In this study, mathematical models of the HCM and LHM were established and solved to describe the heat transfer process during ice hot-point drilling. Case studies were conducted for both the thermal anti-freezing methods to illustrate the characteristics of the required power density and temperature distribution. Finally, the variations in the power density, power consumption, BCT, BCL, and TLT were evaluated for the two thermal anti-freezing methods. The main conclusions of this study are as follows:

(1) The developed HCM and LHM models can be used to calculate the required power density and temperature field during ice hot-point drilling.
(2) The HCM can only be used to drill boreholes with shallow depths or small diameters in temperate ice because of its high-power consumption. Generally, the HCM is recommended for use in ice at temperatures higher than −15 °C. In addition, when the HCM is used, the maximum diameter of the HPD and borehole depth should be less than 70 mm and 150 m, respectively.
(3) Within a reasonable power input, the LHM can be applied to a wide range of ice temperatures, borehole diameters, borehole depths, and ROPs. The HPD with the LHM can be used to drill deep ice boreholes in cold polar plateaus.
(4) For the HCM, the isotherm of the ice during drilling appears as an elongated parabola, whereas the isotherm of ice had a shape similar to that of a spindle for the LHM. The water cavity above the freezing-in HPD for the LHM has a conical shape.
(5) Generally, when the HCM is used, the TLT should be 20–50 times the borehole diameter depending on the working conditions. For the LHM, the TLT can be 5–10 times the borehole diameter.

Table 3
Range analysis for the HCM.

Variables		D (mm)	H (m)	v (m/h)	T_{ice} (°C)
q_0 (W/cm^2)	K_1	0.087	0.116	0.091	0.167
	K_2	0.113	0.109	0.112	0.113
	K_3	0.134	0.108	0.130	0.053
	$\overline{R}$	0.047	0.009	0.038	0.114
	$T_{ice} > D > v > H$				
Q (kW)	K_1	2.679	2.261	3.144	6.763
	K_2	4.461	4.149	5.073	3.849
	K_3	5.354	6.083	4.277	1.880
	$\overline{R}$	2.675	3.821	1.929	4.883
	$T_{ice} > H > D > v$				
δ (mm)	K_1	1524	1223	2401	1680
	K_2	1740	1654	1444	1777
	K_3	1684	2070	1103	1491
	$\overline{R}$	217	847	1298	287
	$v > H > T_{ice} > D$				

Table 4
Design and results of the orthogonal analysis for the LHM.

No.	Variables				Results				
	D (mm)	L (m)	v (m/h)	T_{ice} (°C)	q_0 (W/cm^2)	Q (kW)	t_c (h)	h (m)	δ (mm)
1	80	1	1	−50	0.212	0.762	1.463	1.463	570
2	80	4	3	−30	0.109	1.560	2.853	8.558	613
3	80	7	5	−10	0.033	0.832	10.427	52.136	901
4	120	1	3	−10	0.046	0.264	19.053	57.159	1140
5	120	4	5	−50	0.197	4.480	2.591	12.953	664
6	120	7	1	−30	0.062	2.242	6.738	6.738	1121
7	160	1	5	−30	0.167	1.311	7.249	36.243	761
8	160	4	1	−10	0.019	0.569	35.726	35.726	1637
9	160	7	3	−50	0.130	6.850	4.750	14.251	954

Table 5
Range analysis for the LHM.

Variables		D (mm)	L (m)	v (m/h)	T_{ice} (°C)
q_0 (W/cm^2)	K_1	0.118	0.142	0.098	0.180
	K_2	0.102	0.108	0.095	0.113
	K_3	0.105	0.075	0.132	0.033
	$\overline{R}$	0.017	0.066	0.038	0.147
	$T_{ice} > L > v > D$				
Q (kW)	K_1	1.052	0.779	1.191	4.031
	K_2	2.329	2.203	2.891	1.704
	K_3	2.910	3.308	2.208	0.555
	$\overline{R}$	1.859	2.529	1.700	3.476
	$T_{ice} > L > D > v$				
t_c (h)	K_1	4.914	9.255	14.642	2.935
	K_2	9.461	13.723	8.885	5.613
	K_3	15.909	7.305	6.756	21.736
	R	10.994	6.418	7.887	18.801
	$T_{ice} > D > v > L$				
h (m)	K_1	20.719	31.622	14.642	9.555
	K_2	25.617	19.079	26.656	17.180
	K_3	28.740	24.375	33.777	48.341
	$\overline{R}$	8.021	12.543	19.135	38.785
	$T_{ice} > v > L > D$				
δ (mm)	K_1	695	824	1110	730
	K_2	975	971	902	832
	K_3	1118	992	776	1226
	$\overline{R}$	423	169	334	497
	$T_{ice} > D > v > L$				

(6) Compared with other variables, ice temperature is the main factor affecting the power density, power consumption, BCT, and BCL. Generally, a low ice temperature can result in an increase in the power density and power consumption, whereas cold ice can decrease the BCT and BCL.

Generally, the study systematically modeled the heat transfer when the thermal anti-freezing method is used to prevent the borehole from freezing during ice hot-point drilling. The modeled results are useful for designing heating cables and lateral heaters in ice-drilling engineering. However, all the results were established by modelling. In the future, experimental studies and field experience will be necessary to validate our modelling results.

Authors statement

Yazhou Li: Conceptualization, Methodology, Software, Writing – original draft. **Pavel G. Talalay**: Writing - review & editing. **Xiaopeng Fan**: Writing - review & editing, Investigation. **Da Gong:** Writing - review & editing, Investigation**. Bing Li:** Writing - review & editing, Supervision. **Yuting Ye:** Visualization. **Yue Wang:** Visualization. **Ting Wang:** Visualization.

Declaration of competing interest

The authors declare that they have no known competing financial interests or personal relationships that could have appeared to influence the work reported in this paper.

Data availability

Data will be made available on request.

Acknowledgements

This work was supported by the National Natural Science Foundation of China [grant number 41941005]; the Fundamental Research Funds for the Central Universities [grant numbers 2-9-2021-017, 2-9-2020-015]; and the Ministry of Science and Technology of the People's Republic of China [grant number 2021YFA0719104].

Nomenclature

a, b	Integration constant
C	Heat capacity, J kg^{-1} K^{-1}
D	Diameter of hot-point drill, m
h	Borehole closure length, m
H	Borehole depth, m
k	Thermal conductivity, W m^{-1} K^{-1}
K_1, K_2, K_3	Average of the indicators at each level of the variables
L	Length of hot-point drill
L_m	Latent heat of ice melting, J kg^{-1}
q_0	Power density of heating cable, W m^{-2}
q	Heat flux at borehole wall, W m^{-2}
Q	Power consumption of lateral heater or heating cable, W
r_0	Radius of heating cable, m
R	Borehole radius, m
R_0	Radius of thermal head, m
$\overline{R}$	Range in sensitivity analysis
t	Time, s
t_c	Borehole closure time, s
T_i	Ice temperature, K
T_{ice}	Original ice temperature, K
T_{i_2D}	Ice temperature in the two-dimensional model, K
T_{i_1D}	Ice temperature in the one-dimensional model, K
T_w	Water temperature, K
T_m	Melting point temperature, K
v	Rate of penetration, m s^{-1}
o-rz	Cylindrical coordinate system

Greek Symbols

α	Thermal diffusivity, m^2 s^{-1}
ρ	Density, kg m^{-3}

δ	Thickness of thermal ice layer, m
∞	Infinity, m

Subscripts

water	w (ρ_w, C_w, k_w, α_w, θ_w)
ice	i (ρ_i, C_i, k_i, α_i, θ_i)

Abbreviations

BCL	Borehole Closure Length
BCT	Borehole Closure Time
HCM	Heating Cable Method
HPD	Hot Point Drill
LHM	Lateral Heating Method
ROP	Rate of Penetration
TLT	Thermal Layer Thickness

References

[1] A. Nizery, Electrothermic rig for the boring of glaciers, Eos Transactions American Geophysical Union 32 (1951) 66–72, https://doi.org/10.1029/TR032i001p00066.
[2] J.A.F. Gerrard, M.F. Perutz, A. Roch, Measurements of the velocity distribution along a vertical line through a glacier, Proc. R. Soc. A 213 (1952) 546–558, https://doi.org/10.1098/rspa.1952.0144.
[3] F. Gillet, Steam, hot-water and electrical thermal drills for temperate glaciers, J. Glaciol. 14 (1975) 171–179, https://doi.org/10.1017/S0022143000013484.
[4] B. Rle, Hooke, University of Minnesota ice drill, in: Ice-Core Drilling: Proceeding of the Symposium in, University of Nebraska Lincoln, 1976.
[5] F.A. Wade, The physical aspects of the Ross Shelf ice, Proc. Am. Phil. Soc. 89 (1945) 160–173.
[6] P.G. Talalay, Hot-point drills, in: P.G. Talalay (Ed.), Thermal Ice Drilling Technology, Springer Singapore, Singapore, 2020, pp. 1–80.
[7] I.A. Zotikov, The Thermophysics of Glaciers, D. Reidel Pub. Co., Dordrecht, 1986.
[8] K. Zacny, G. Paulsen, Y. Bar-Cohen, X. Bao, M. Badescu, H.J. Lee, S. Sherrit, V. Zagorodnov, L. Thompson, P.G. Talalay, Drilling and breaking ice, in: Y. Bar-Cohen (Ed.), Low Temperature Materials and Mechanisms, CRC Press, 2016, pp. 271–347, https://doi.org/10.1201/9781315371962.
[9] H.T. Ueda, D.E. Garfield, The USA CRREL drill for thermal coring in ice, J. Glaciol. 8 (1969) 311–314, https://doi.org/10.1017/S0022143000031282.
[10] V.S. Zagorodnov, V.A. Morev, O.V. Nagornov, J.J. Kelley, B.R. Koci, Hydrophilic liquid in glacier boreholes, Cold Reg. Sci. Technol. 22 (1994) 243–251, https://doi.org/10.1016/0165-232X(94)90003-5.
[11] M. Grześ, Non-cored hot point drills on Hans Glacier (Spitsbergen), method and first results, Pol. Polar Res. 1 (1980) 75–85.
[12] F. Gillet, C. Rado, G. Marec, M. Maitre, J. Perrin, "Climatopic" thermal probe, in: Proceeding of the Second International Workshop/symposim on Ice Drilling Technology, 1982, 1984.
[13] M. Zeibig, G. Delisle, Drilling into Antarctic ice - the new BGR ice drill, Polarforschung 62 (1994) 147–150.
[14] P. Talalay, B. Liu, Y. Yang, X. Fan, J. Hong, D. Gong, M. Sysoev, X. Li, Y. Li, Electric thermal drills for open-hole coring in ice, Pol. Sci. 17 (2018) 13–22, https://doi.org/10.1016/j.polar.2018.05.007.
[15] D.F. Classen, Thermal Drilling and Deep Ice-Temperature Measurements on the Fox Glacier, Yukon, A Thesis Submitted in Partial Fulfillment of the Requirements for the Degree of Master of Science, Department of Geophysics, The University of British Columbia, Canada, 1970.
[16] Y. Suto, S. Saito, K. Osada, H. Takahashi, H. Motoyama, Y. Fujii, Y. Tanaka, Laboratory experiments and thermal calculations for the development of a next-generation glacier-ice exploration system: development of an electro-thermal drilling device, Pol. Sci. 2 (2008) 15–26, https://doi.org/10.1016/j.polar.2008.02.002.
[17] P.G. Talalay, V.S. Zagorodnov, A.N. Markov, M.A. Sysoev, J. Hong, Recoverable autonomous sonde (RECAS) for environmental exploration of Antarctic subglacial lakes: general concept, Ann. Glaciol. 55 (2014) 23–30, https://doi.org/10.3189/2014AoG65A003.
[18] B. Dachwald, J. Mikucki, S. Tulaczyk, I. Digel, C. Espe, M. Feldmann, G. Francke, J. Kowalski, C. Xu, IceMole: a maneuverable probe for clean in situ analysis and sampling of subsurface ice and subglacial aquatic ecosystems, Ann. Glaciol. 55 (2014) 14–22, https://doi.org/10.3189/2014AoG65A004.
[19] D. Heinen, J. Audehm, F. Becker, G. Boeck, C. Espe, M. Feldmann, G. Francke, P. Friend, N. Haberberger, K. Helbing, C.T. Nghe, M. Stelzig, M. Vossiek, C. Wiebusch, S. Zierke, The TRIPLE melting probe - an electro-thermal drill with a forefield reconnaissance system to access subglacial lakes and oceans, in: OCEANS 2021, 20-23 Sept., 2021, San Diego, CA, USA, 2021, pp. 1–7, https://doi.org/10.23919/OCEANS44145.2021.9705999.
[20] H.W.C. Aamot, The Philberth probe for investigating polar ice caps, USA CRREL Special Report 119 (1967).
[21] J.R. Kelty, An in Situ Sampling Thermal Probe for Studying Global Ice Sheets, A Thesis Submitted in Partial Fulfillment of the Requirements for the Degree of Doctor of Philosophy, Graduate College in the University of Nebraska, Nebraska, Lincoln, USA, 1995.
[22] Y. Li, Y. Yang, X. Fan, X. Li, P.G. Talalay, Power consumption of a Philberth thermal probe in ice sheet exploration, Cold Reg. Sci. Technol. 177 (2020), 103114, https://doi.org/10.1016/j.coldregions.2020.103114.
[23] T.A. Gosink, B.R. Koci, J.J. Kelley, Aqueous ethanol as an ice-drilling fluid, J. Glaciol. 39 (1993) 703–705, https://doi.org/10.1017/S0022143000016610.
[24] V.S. Zagorodnov, J.J. Kelley, O.V. Nagornov, Drilling of glacier boreholes with a hydrophilic liquid, Mem. Natl. Inst. Polar Res. 49 (1994) 153–164.
[25] V.S. Zagorodnov, L.G. Thompson, J.J. Kelley, B. Koci, V. Mikhalenko, Antifreeze thermal ice core drilling: an effective approach to the acquisition of ice cores, Cold Reg. Sci. Technol. 28 (1998) 189–202, https://doi.org/10.1016/S0165-232X(98)00019-6.
[26] B. H Hills, D.P. Winebrenner, W.T. Elam, P.M.S. Kintner, Avoiding slush for hot-point drilling of glacier boreholes, Ann. Glaciol. 62 (2020) 166–170, https://doi.org/10.1017/aog.2020.70.
[27] H.W.C. Aamot, Heat transfer and performance analysis of a thermal probe for glaciers, USA CRREL Tech. Rep. 194, 1967b.
[28] S. Ulamec, J. Biele, O. Funke, M. Engelhardt, Access to glacial and subglacial environments in the Solar System by melting probe technology, Rev. Environ. Sci. Biotechnol. 6 (2007) 71–94, https://doi.org/10.1007/s11157-006-9108-x.
[29] S. DiPippo, R. Mugnuolo, P. Vielmo, W. Prendin, The exploitation of Europa ice and water basins: an assessment on required technological developments, on systems design approaches and on relevant expected benefits to space and Earth based activities, Planet. Space Sci. 47 (1999) 921–933, https://doi.org/10.1016/S0032-0633(99)00012-4.
[30] N.I. Kömle, G. Kargl, M. Steller, Melting probes as a means to explore planetary glaciers and ice caps, in: Proceedings of the First European Workshop on Exo/Astrobiology, 2002.
[31] R.D. Lorenz, Thermal drilling in planetary ices: an analytic solution with application to planetary protection problems of radioisotope power sources, Astrobiology 12 (2012) 799–802, https://doi.org/10.1089/ast.2012.0816.

[32] W. Christoph, F. Oliver, The TRIPLE/nanoAUV initiative a technology development initiative to support astrobiological exploration of ocean worlds, CEAS Space Journal 12 (2020) 115–122, https://doi.org/10.1007/s12567-019-00275-7.
[33] A.A. Memon Usman, H. Anwaar, T. Muhammad, A.A. Alharbi, A.S. Alshomrani, Y.R. Aladwani, A forced convection of water-aluminum oxide nanofluids in a square cavity containing a circular rotating disk of unit speed with high Reynolds number: a Comsol Multiphysics study, Case Stud. Therm. Eng. 39 (2022), 102370, https://doi.org/10.1016/j.csite.2022.102370.
[34] M.M Bhatti Usman, Abuzar Ghaffari, M. H Doranehgard, The role of radiation and bioconvection as an external agent to control the temperature and motion of fluid over the radially spinning circular surface: a theoretical analysis via Chebyshev spectral approach, Math. Methods Appl. Sci. (2022) 1–18, https://doi.org/10.1002/mma.8085.
[35] Y.M. Li, K. Al-Khaled, S. Gouadria, E.R. El-Zahar, Usman, S.U. Khan, M.I. Khan, M.Y. Malik, Numerical Simulations for Three-Dimensional Rotating Porous Disk Flow of Viscoelastic Nanomaterial with Activation Energy, Heat Generation and Nield Boundary Conditions, Wave Random Complex, 2022, pp. 1–20, https://doi.org/10.1080/17455030.2022.2029614.
[36] N. Humphrey, K. Echelmeyer, Hot-water drilling and bore-hole closure in cold ice, J. Glaciol. 36 (1990) 287–298, https://doi.org/10.3189/002214390793701354.
[37] A.A. Khan, N. Abbas, S. Nadeem, Q. Shi, M.Y. Malik, M. Ashraf, S. Hussain, Non-Newtonian based micropolar fluid flow over nonlinear starching cylinder under Soret and Dufour numbers effects, Int. commun. heat mass 127 (2021), 105571, https://doi.org/10.1016/j.icheatmasstransfer.2021.105571.
[38] N. Abbas, S. Nadeem, M.N. Khan, Numerical analysis of unsteady magnetized micropolar fluid flow over a curved surface, J. Therm. Anal. Calorim. 147 (2022) 6449–6459, https://doi.org/10.1007/s10973-021-10913-0.
[39] N. Abbas, W. Shatanawi, Heat and mass transfer of micropolar-Casson nanofluid over vertical variable stretching Riga sheet, Energies 15 (2022) 4945, https://doi.org/10.3390/en15144945.
[40] K.M. Cuffey, W.S.B. Paterson, The Physics of Glaciers, fourth ed., Butterworth-Heinemann, Oxford, 2010.